Acta Crystallographica Section A
Foundations of Crystallography
ISSN 0108-7673

Received 10 October 2000
Accepted 9 November 2000

Diffuse X-ray scattering and strain effects in disordered crystals

T. R. Welberry

Research School of Chemistry, Australian National University, Canberra, ACT 0200, Australia. Correspondence e-mail: welberry@rsc.anu.edu.au

It is shown in this paper that a feature that has been observed in the diffuse scattering patterns of a wide variety of different materials – a diffuse 'ring' or 'doughnut'-shaped region of scattering – can be understood in terms of a simple model that has been borrowed from the field of sol–gel science. In this, it is supposed that there is a balance between the local attractive forces that are trying to make a particular structure and a rather longer range repulsive force. In the present context, it is believed that this latter force has its origin in the strain that builds as the preferred local structure tries to fit into the average crystal lattice. Simple Monte Carlo (MC) computer simulations are described that demonstrate this principle for three example materials: cubic stabilized zirconia, the *p*-didecylbenzene/urea inclusion compound and the pure molecular compound 1,3-dibromo-2,5-diethyl-4,6-dimethylbenzene, $C_{12}H_{16}Br_2$ (BEMB2).

1. Introduction

In numerous recent studies, we have observed diffuse X-ray scattering from a wide variety of materials. Although these studies have shown the great diversity of diffuse scattering patterns that can exist in different materials, some commonly occurring features have also emerged. One particularly distinctive feature that has been observed in several quite different materials is a diffuse 'ring' or 'doughnut'-shaped region of scattering, with a dark (or low-intensity) centre. In Figs. 1(*a*), (*b*) and (*c*), we show regions of the diffraction patterns of the aluminosilicate ceramic mullite (see Welberry & Withers, 1990; Butler & Welberry, 1994), a cubic stabilized zirconia (see Welberry *et al.*, 1993, 1995) and the inclusion compound didecylbenzene/urea (see Mayo *et al.*, 1998), which all show such features. In Fig. 1(*d*), we show a region of the diffraction pattern of the pure molecular crystal 1,3-dibromo-2,5-diethyl-4,6-dimethylbenzene, in which a dark 'hole' appears in a broader region of diffuse scattering (see Welberry & Siripitayananon, 1987). We consider that this feature is closely related to the diffuse 'rings' that are apparent in the other materials.

In metal alloys, diffuse rings of this kind have been attributed to spinodal decomposition (Cahn, 1967) but more recently Butler & Hanley (1999) have shown that such features in the diffraction patterns of sol–gel systems can arise from competition between a short-range attractive and a long-range repulsive potential. In the present paper, we discuss how these basic concepts can be carried over from these sol–gel systems to provide insight into the mechanisms governing disorder in the different crystalline materials mentioned above.

In §2, we use the potentials described by Butler & Hanley and apply them to systems of particles on a simple (square) lattice, in order to show that the diffuse 'ring' effects carry over from continuous media systems to ones where the interacting particles are confined to a crystal lattice. In the subsequent sections, we show how the same basic principles may be used to describe the effects observed in cubic stabilized zirconias, the inclusion compound didecylbenzene/urea and the pure molecular crystal system 1,3-dibromo-2,5-diethyl-4,6-dimethylbenzene. Mullite, the other system depicted in Fig. 1, is omitted from the present discussion because in that system more complex considerations are involved. For example, in the 0.5**c*** section, incommensurate modulations with a wavevector $\mathbf{q} = 0.5\mathbf{c}^* + 0.3\mathbf{a}^*$ are observed, while in the 0.16**c*** section there appears to be a tendency to form an incommensurate modulation with a wavevector in the *b** direction.

2. Simulations on a square lattice

A square lattice, of cell constant a_0 and consisting of 256×256 sites, was set up in the computer with 35% of sites occupied by particles at random. The particles were then allowed to interact *via* a Lennard-Jones potential, $U_{ij} = a(1/r^{12} - 1/r^6)$. The minimum in this potential occurs at $r \simeq 1.1r_0$, where r_0 corresponds to the point where the steep repulsive part of the curve passes through zero (see Fig. 2). In order to provide that the cell spacing corresponded to the minimum of the potential, the distance variable r was measured on a scale such that $a_0 = 1.1r_0$. The energy used in the Monte Carlo (MC) simulation was

$$E = \sum_{\substack{\text{vectors } r_{ij} \\ r_{ij} \leq 10a_0}} \frac{U_{ij}}{kT} = \sum_{\substack{\text{vectors } r_{ij} \\ r_{ij} \leq 10a_0}} \frac{a}{kT}\left(\frac{1}{r_{ij}^{12}} - \frac{1}{r_{ij}^{6}}\right). \quad (1)$$

Monte Carlo simulation was carried out using cyclic boundary conditions for 10000 cycles of iteration, where a cycle is defined as that number of individual MC steps required to visit each particle once on average. A value of $kT = 0.32$ was used throughout. The configuration was saved after 50, 1000 and 10000 cycles and the diffraction pattern of each of these distributions was obtained using a fast Fourier transform (FFT) algorithm. Fig. 3 shows both the real-space distributions and the corresponding FFT for these three stages of the iteration. The region of reciprocal space shown in each of these FFT figures corresponds to $\pm h/2$, $\pm k/2$ with the origin in the centre. It is seen that, as the iteration progresses, particles (black) tend to aggregate and the domain size (of black and white regions) becomes increasingly coarse, so that eventually it would be supposed that complete phase separation takes place. At the same time, the FFT shows a diffuse ring of scattering, the radius of which corresponds to the reciprocal of the average distance between domains. After a large number of iterations, the circle becomes very small and with eventual phase separation will disappear into the Bragg-peak position.

To compare with the Lennard-Jones potential, Butler & Hanley (1999) also used a potential, the so-called 6-2-12 potential,

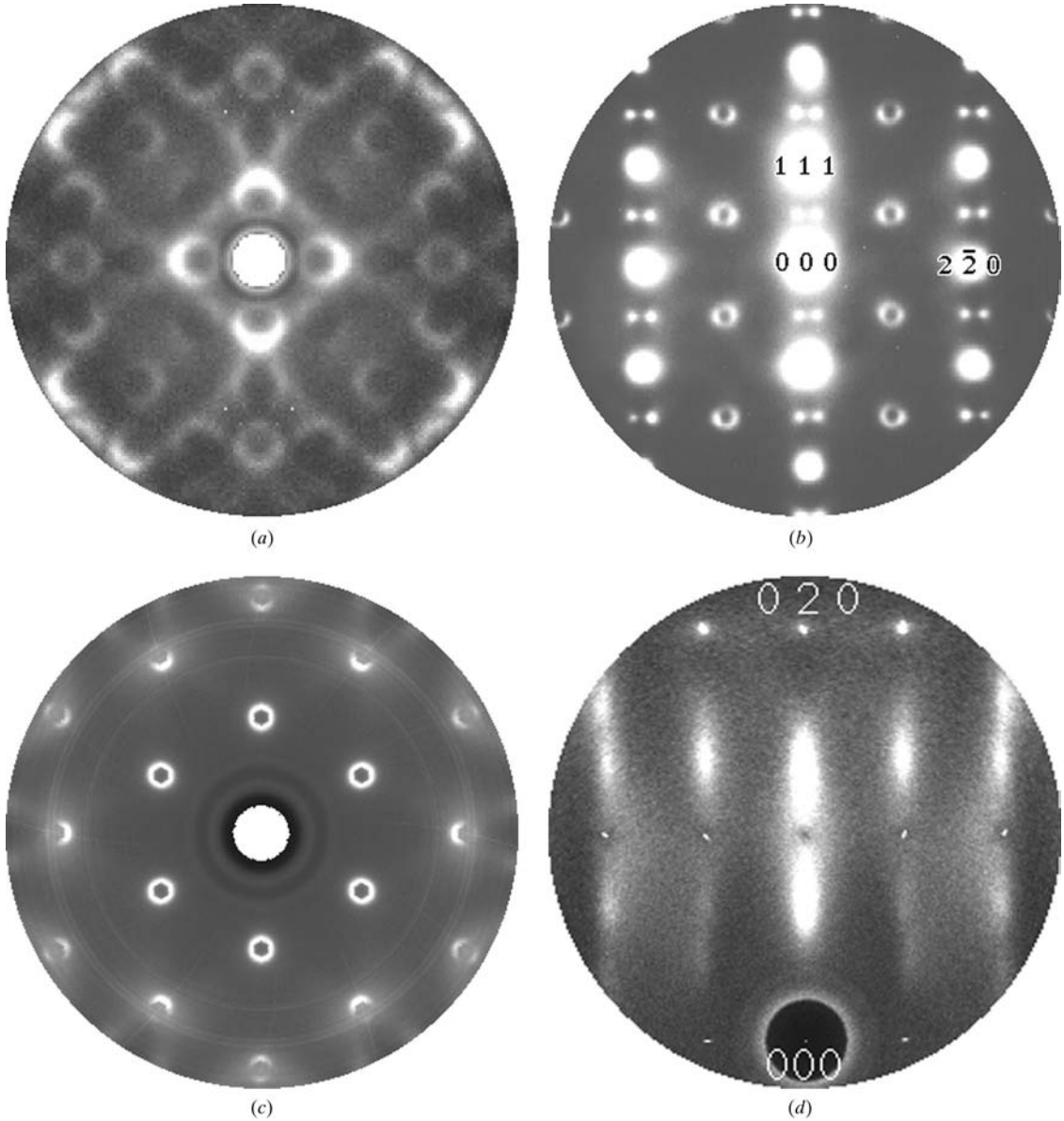

Figure 1
Sections of the diffraction patterns of various materials exhibiting 'diffuse rings' of scattering. (*a*) The 0.7*c** section of the X-ray diffraction pattern of mullite. (*b*) [11$\bar{2}$] zone-axis electron diffraction pattern of a CSZ. (*c*) *p*-Didecylbenzene–urea inclusion compound, (*hk*0.35). (*d*) Region around 010 of the (*hk*$\bar{h}$) X-ray diffraction pattern of 1,3-dibromo-2,5-diethyl-4,6-dimethylbenzene.

$$U_{ij} = a\left(\frac{1}{r^{12}} + \frac{b}{r^2} - \frac{(1+b)}{r^6}\right), \qquad (2)$$

which incorporates a mildly repulsive r^{-2} term. The value of b used was 0.15. Note that when $b = 0.0$ the function reverts to the simple Lennard-Jones potential. The two functions are compared in Fig. 2.

When the function (2) is used in the MC simulation (see Fig. 4), the behaviour is initially similar to the straight Lennard-Jones case. However, after some coarsening of the domain structure with a corresponding decrease in the radius of the diffuse ring in the FFT, a stable domain structure ensues with no further coarsening taking place even after a very large number of MC cycles. The diffuse circle in the FFT attains a stable radius. It is clear that for this system the tendency to aggregate induced by the r^{-6} term is countered by the rather longer range, though mild, r^{-2} repulsion term.

In the following sections, we suppose that the general principle demonstrated by the simple example given in this section is a commonly occurring theme in real materials. *I.e.* the diffuse rings that are observed in these materials are symptomatic of the fact that at short distances the interatomic or intermolecular interactions are trying to form a particular structure but at rather longer distances a repulsion term comes into play that limits the extent that the preferred short-range structure can propagate. It is our tenet that this repulsion term results from the accumulated strain induced by local misfits of the disordered species. For a rigorous treatment of this problem, it would be necessary to use proper interatomic interactions extending over large distances. This would be a formidable computational problem even using potentials as simple as (2), and this has not been attempted. For the present purpose, which is primarily to demonstrate the principle, we reduce the particular problems to their barest essentials. In each of the examples described, we use an attractive potential invented for the purpose of reproducing the preferred short-range structure, and a much simplified repulsive potential based on an average measure of the induced strain.

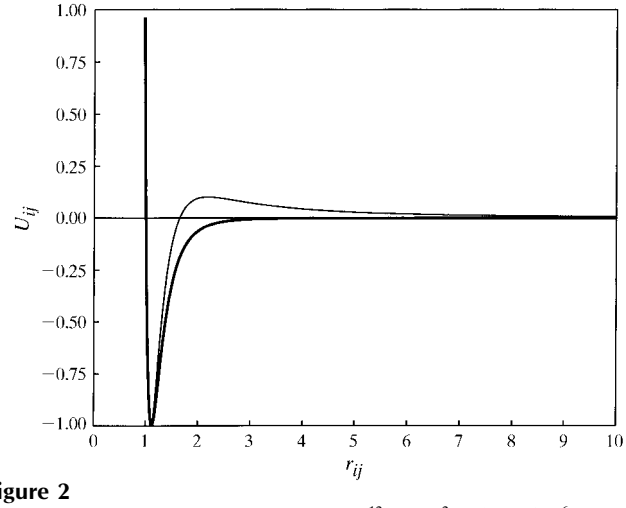

Figure 2
Plot of the potential function, $U_{ij} = a[1/r^{12} + b/r^2 - (1+b)/r^6]$, used in the MC simulations. The heavy line corresponds to the normal Leonard-Jones potential when $a = 4.0$ and $b = 0.0$. The thin line corresponds to the 6-2-12 potential used when $a = 4.8249$ and $b = 0.15$.

3. Diffuse rings in cubic stabilized zirconias

3.1. Background

Cubic stabilized zirconias are based on the simple fluorite structure (see Fig. 5*a*). In the disordered CSZ's the cation sites are disordered but fully occupied by Zr or the stabilizing cation such as Y or Ca, while a fraction of the oxygen sites are vacant. The structure of CSZ's has been the subject of a large number of publications by numerous authors over a period of many years (Allpress & Rossell, 1975; Rossell & Scott, 1977; Morinaga *et al.*, 1980; Suzuki *et al.*, 1985; Neder *et al.*, 1990). Although greater understanding of the structure has been forthcoming more recently (Welberry *et al.*, 1993, 1995), a completely satisfactory model for the disorder is still not available. It is clear that a completely satisfactory model should describe both the distribution of the disordered cations and the anion vacancies, but also the way in which atoms are mutually displaced from their average lattice sites. X-ray diffraction patterns are extremely complex and are dominated by atomic displacements which arise as the result of cation relaxation around the oxygen vacancy sites. Electron diffraction patterns, on the other hand, often appear relatively simple and consist of a series of diffuse rings such as those seen in Fig. 1(*a*). This simplicity largely occurs because, for electron diffraction, multiple scattering tends to average out azimuthal variations of intensity that are due to different displacement directions. The distribution of scattered intensity in electron diffraction, therefore, tends more to reflect the nature of the ionic occupancy distributions.

Based on the observation that in many fluorite-related superlattice phases a commonly occurring feature is a pair of oxygen vacancies separated by $\frac{1}{2}\langle 111\rangle$ across a cation site, we based a previous model for ionic ordering (Welberry *et al.*, 1993) on the supposition that the driving force was a preference for such $\frac{1}{2}\langle 111\rangle$ vacancy pairs and an avoidance of $\frac{1}{2}\langle 110\rangle$ and $\frac{1}{2}\langle 100\rangle$ vacancy pairs. In that model, which was developed mainly in the context of yttrium-stabilized zirconia, little information could be deduced about the distributions of Y and Zr since these have virtually identical X-ray scattering factors. In the present case, we concentrate solely on the distribution of cations and suppose that further work will be capable of describing oxygen–vacancy distributions, taking into account valence requirements and local charge balance.

The diffuse circles that may be seen in Fig. 1(*b*), both as distinct circles and as pairs of peaks (owing to intersection with the Ewald sphere of circles in other orientations), occur throughout reciprocal space in the neighbourhood of $\frac{1}{2}\langle 111\rangle^*$ reciprocal positions, as shown in Fig. 5(*b*). To construct a model, therefore, we suppose that what is occurring is that the structure is locally trying to order to make a superlattice that will have a superlattice peak at these $\frac{1}{2}\langle 111\rangle^*$ reciprocal positions, but that induced strain prevents this ordering becoming long range.

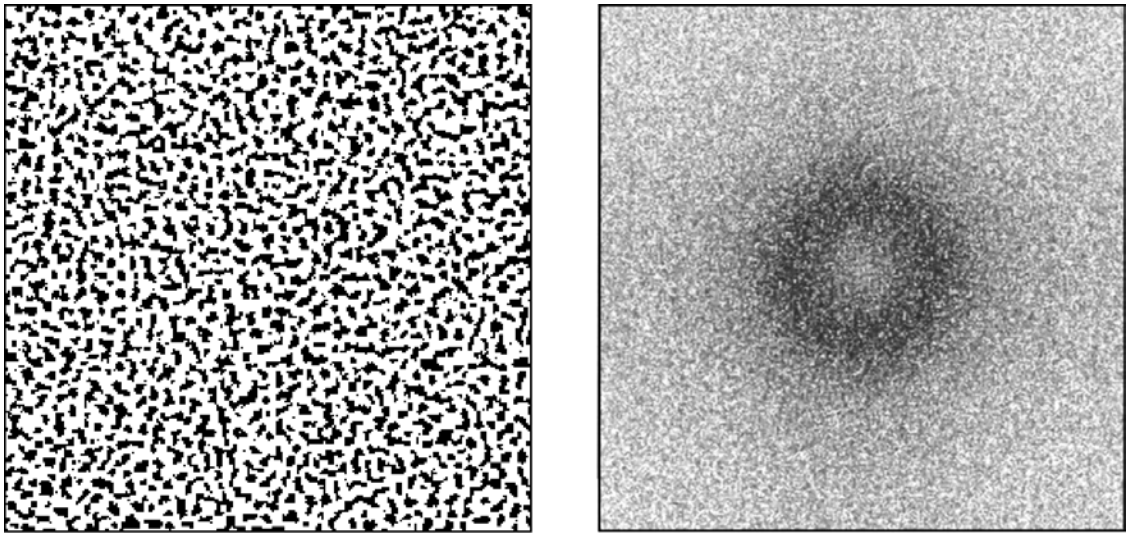

(*a*) 50 MC cycles

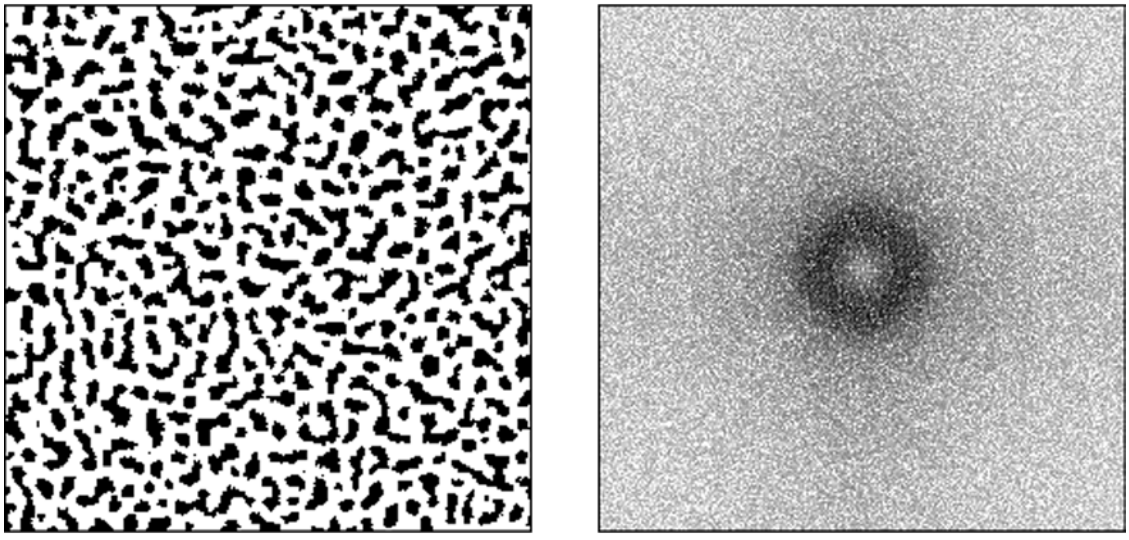

(*b*) 1000 MC cycles

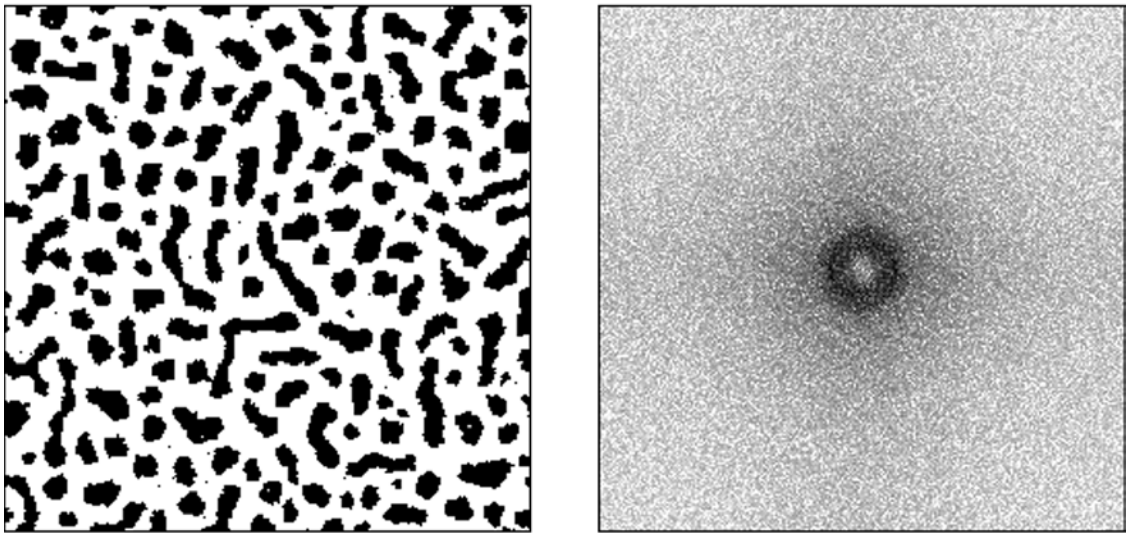

(*c*) 10000 MC cycles

Figure 3
Lennard-Jones potential. 256 × 256 lattice and diffraction patterns (FFT).

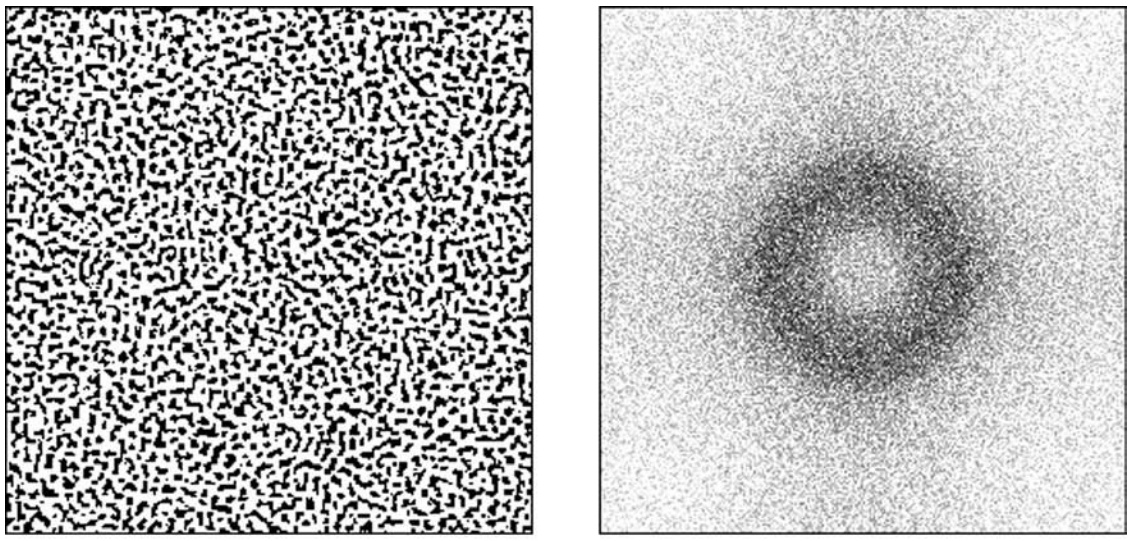

(*a*) 50 MC cycles

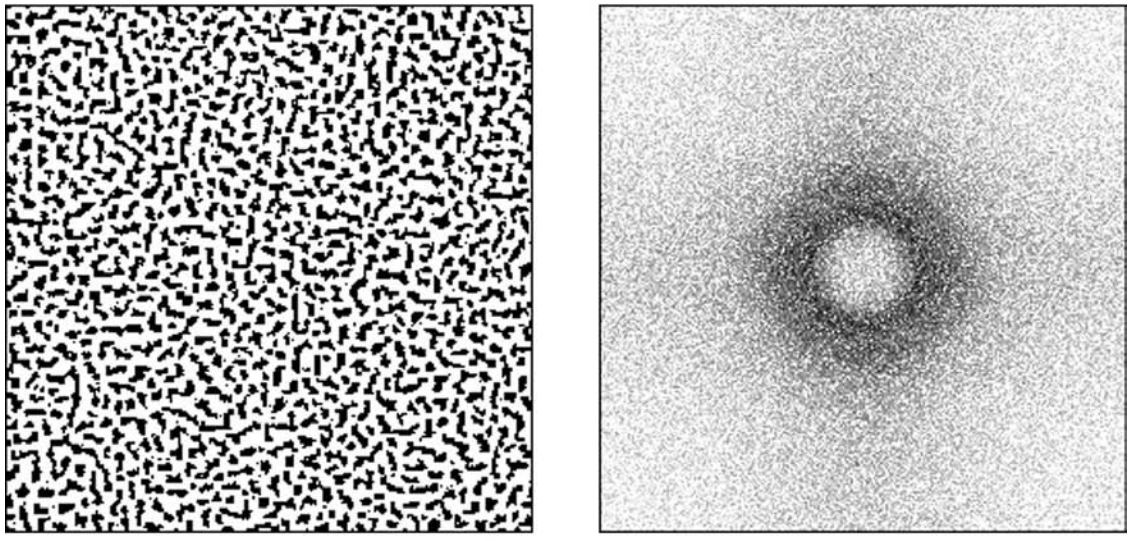

(*b*) 1000 MC cycles

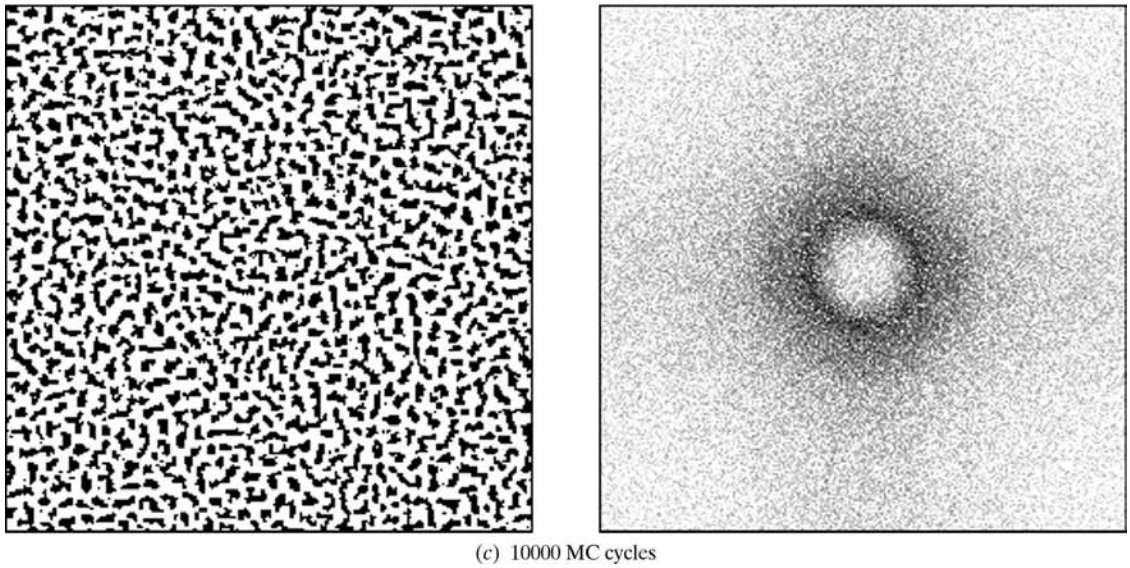

(*c*) 10000 MC cycles

Figure 4
6-2-12 potential. 256 × 256 lattice and diffraction patterns (FFT).

3.2. Monte Carlo model

A commonly occurring fluorite-related superlattice phase is that of the pyrochlore structure of general stoichiometry $A_2B_2O_7$. This superstructure gives rise to extra Bragg peaks at the $\frac{1}{2}\langle 111\rangle^*$ reciprocal positions of the fluorite parent cell. We therefore conjecture that it is the pyrochlore phase that the CSZ is attempting to form. In the (cubic) pyrochlore structure, the A and B cations are ordered to produce a $2 \times 2 \times 2$ superlattice. Successive layers of cations viewed down [100] are shown in Fig. 5(*c*). It is seen that in the first layer [110] rows of A cations alternate with parallel rows of B cations. In the second layer, similar alternating rows are oriented along $[1\bar{1}0]$. Where the rows of cations in the two layers cross, there are tetrahedra of like cations, which are a characteristic feature of the structure.

For the purposes of the present work, we require a suitable short-range potential, for use in a MC simulation, which will lead to the formation of the pyrochlore structure if no other forces are present. The simple potential we adopted for this purpose was one based on the relative energy of different types of cation clusters. In Fig. 5(*d*), we show five different cation arrangements (labelled A–E) for the nearest-neighbour tetrahedral clusters (mentioned above) as well as six different cation arrangements (labelled F–K) for the next-nearest-neighbour cation square clusters. Energies E_i were assigned to the different clusters shown in Fig. 5(*d*). The aim in assigning these energies was to favour the tetrahedral clusters A and B containing four like cations and the square clusters which contained two of each type of cation, clusters H and K. These energies were: $E_A = E_B = -1$; $E_C = E_D = E_E = 0$; $E_F = E_I = +4$; $E_G = E_J = +1$; $E_H = E_K = 0$. These energies are on a scale relative to the simulation temperature of $kT = 2.0$, which was used throughout. Then the local structure contribution to the energy is

$$E_{\rm local} = \sum_{\rm n.n.tetrahedra} (E_i) + \sum_{\rm n.n.n.squares} (E_i). \qquad (3)$$

In order to understand why a strain term in the energy might give rise to diffuse circles normal to each $\langle 111\rangle$ direction, we show in Fig. 6 the cation distribution in pyrochlore for two consecutive close-packed layers normal to [111]. It is seen that in the first layer single A cations are surrounded by six B cations, while in the next layer six A cations surround a single B cation. It is clear from this that if the two ions have substantially different sizes (taking into account the surrounding anions needed to satisfy their valence requirements), then there will be a mismatch in the sizes of the two layers. It would, therefore, be expected that a strain energy would build up as the size of pyrochlore domains increases. To model this in a very simple way, we supposed the strain energy to depend on the ratio of A to B cations within a radius r_s of a given cation. Initially, r_s was set to 3× the nearest-neighbour cation distance, as indicated by the large circles in Fig. 6. If n_A and n_B are the respective numbers of A and B cations within r_s of a given cation, the contribution to the MC energy was taken as

$$E_{\rm strain} = K_s \left[\frac{(n_A - n_B)}{(n_A + n_B)}\right]^2. \qquad (4)$$

The force constant K_s was used to gradually introduce increasing amounts of strain into successive simulation runs. Note that strain terms of the type (4) occur on all four orientations of the {111} planes simultaneously.

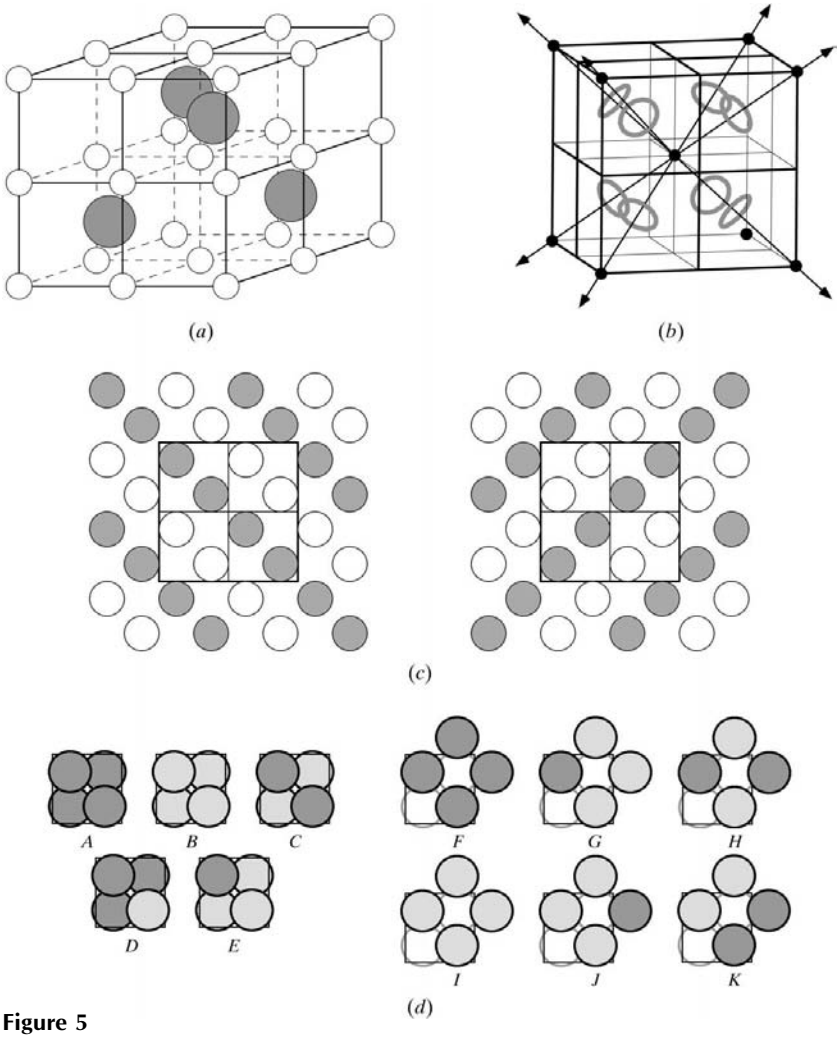

Figure 5
(*a*) The fluorite structure. (*b*) The position of the diffuse circles in the diffraction patterns of CSZ's. (*c*) Successive [100] layers of cations in the pyrochlore structure. The large square is the pyrochlore unit cell and the small square is the fluorite parent cell. (*d*) The nearest-neighbour tetrahedral clusters, A–E, and next-nearest-neighbour square clusters, F–K, used in the potential used to generate the pyrochlore structure.

3.3. Simulation results for CSZ's

Monte Carlo simulation was carried out using an array of $32 \times 32 \times 32$ fluorite unit

cells. Since computation of the strain energy is computationally intensive, iteration was carried out for only ~200 MC cycles. In Fig. 7, we show the resulting real-space distributions of cations on a typical (111) plane from the 3D simulations for different simulations. Alongside each figure, we show corresponding $\frac{1}{2}\langle 111\rangle^*$ sections of the diffraction patterns calculated from the simulations using the program *DIFFUSE* (Butler & Welberry, 1992). For all three examples, the strain radius, r_s, was taken as 3× the nearest-neighbour cation distance. For Fig. 7(*a*), the force constant K_s was 5.0, for Fig. 7(*b*) it was 15.0 and for Fig. 7(*c*) it was 25.0. Fig. 7(*a*) clearly indicates that large domains of the pyrochlore structure exist and this is borne out in its diffraction pattern, where only slightly broadened Bragg peaks exist at the $\frac{1}{2}\langle 111\rangle^*$ reciprocal positions. For Fig. 7(*b*), the diffuse peaks have become broader with some definite ellipsoidal shape, while for Fig. 7(*c*) the peaks have resolved into definite diffuse circles (and pairs of spots corresponding to the intersection of the Ewald sphere with diffuse circles oriented out of the plane). It is interesting to note that, while some small regions of the pyrochlore structure can be seen in Fig. 7(*b*) (see example outlined), none can be recognized in Fig. 7(*c*).

4. Diffuse circles in didecylbenzene/urea inclusion compound

4.1. Background

Urea acts as the host for a large number of different long-chain molecular guests, not least of which are the *n*-alkanes, which have been studied over a period of many years. In a recent study, we surveyed a system in which a series of dialkylbenzene molecules were used as guests in order to investigate the ability of urea to accommodate the bulky benzene group, which is rather too large for the urea channels (see Mayo *et al.*, 1998). Of these compounds, didecylbenzene (see Fig. 8*a*) gave particularly interesting diffraction results, including the section of diffuse scattering shown in Fig. 1(*c*). In common with many other urea inclusion compounds, the long-chain guests form pseudo 1D crystals within each urea channel, giving rise to diffuse planes of scattering normal to the channel axis with the spacing of the planes incommensurate with the urea *c*-axis repeat. Fig. 1(*c*) represents the distribution of intensity within the first (and sharpest) of these diffuse planes, which was labelled 'd1' in Mayo *et al.* (1998). [Note that there is no zero-level diffuse plane because in projection down the channel axis all different orientations of the 'footprint' are superposed, so producing the same scattering from each channel.] The presence of structure in this plane indicates that there is strong interaction between the molecular behaviour in adjacent channels.

4.2. Monte Carlo model

The *n*-alkanes fit rather loosely into the urea channels (see Fig. 8*b*) so that at low temperature the channels tend to distort into an orthorhombic cell with alkane orientations in neighbouring channels inclined to each other in a herring-bone arrangement (see Welberry & Mayo, 1996). The fact that the diffuse rings of scattering in the d1 layers of didecylbenzene/urea tend to occur around integral h, k positions indicates that the guests in neighbouring channels in this compound tend to have the same orientation. The 'footprint' of didecylbenzene (*i.e.* the shape of the molecule projected down its long axis) is much more elongated than that of the *n*-alkanes however and will not fit into the urea without a unidirectional elongation of the hexagonal channel cross section. The only way for such elongated hexagons to pack is if they are all oriented in the same direction. We imagine, therefore, that locally the structure is trying to make domains as depicted in Fig. 8(*c*), of which there are three symmetry-related versions.

As seen from this figure, the formation of such domains will produce strain in the hexagonal parent structure, the larger the domain the larger the strain. We thus have an analogous situation to the previous CSZ example. Locally, the elongated 'footprint' of the guest is trying to make a structure in which all the guests are aligned parallel to each other but the strain that is induced in the hexagonal host lattice tends to suppress this happening over a long range. As before, we use simple energy functions $E_{\rm local}$ and $E_{\rm strain}$ to represent these opposing interactions. In this case, we use

$$E_{\rm local} = \sum_{\substack{\text{nearest}\\ \text{neighbours}}} \delta(\sigma_i, \sigma_j). \qquad (5)$$

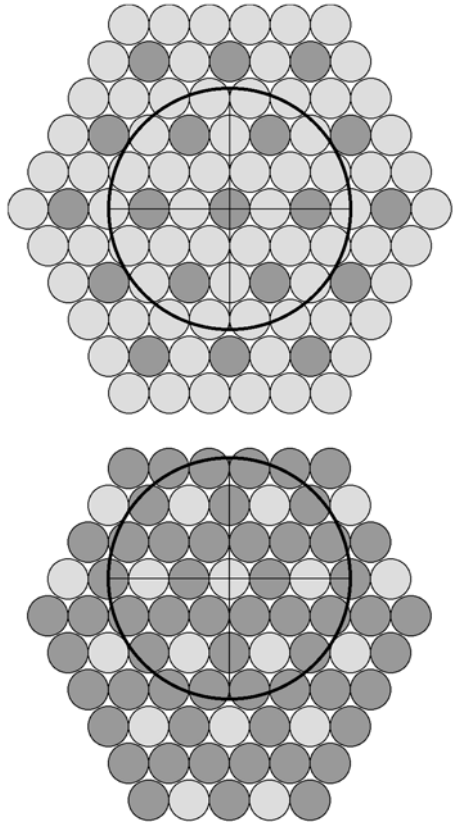

Figure 6
Successive close-packed layers of cations in planes normal to ⟨111⟩ in pyrochlore. A strain energy is assumed to depend on the ratio of the number of A and B cations within a radius r_s of a given cation.

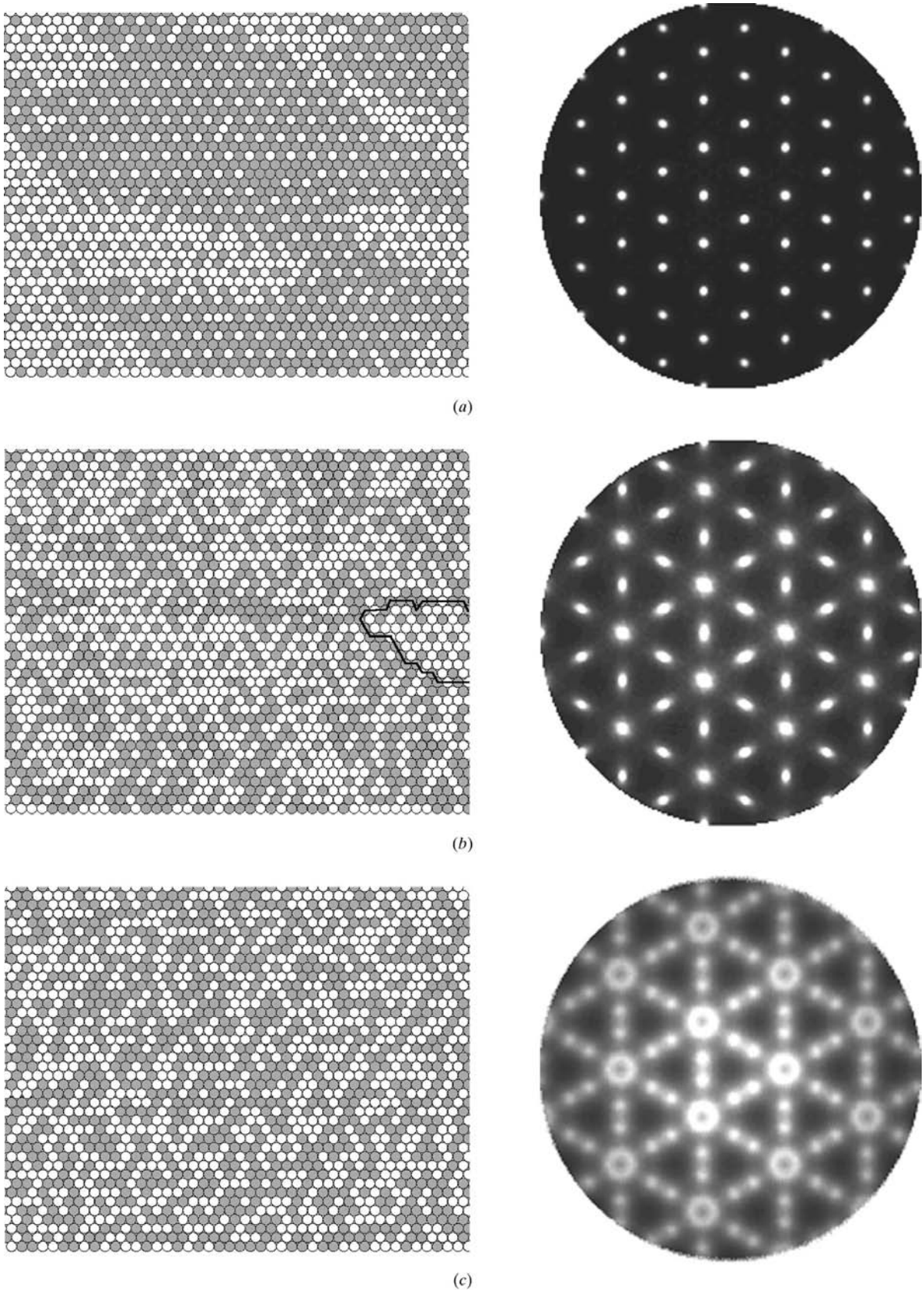

Figure 7
Example regions of the close-packed planes of cations normal to [111] in CSZ, taken from three MC simulations which had different values of the strain term constant K_s. For (*a*), $K_s = 5$; for (*b*), $K_s = 15$; for (*c*), $K_s = 25$. On the right is the corresponding diffraction pattern of the $\frac{1}{2}\langle 111\rangle^*$ reciprocal section calculated from the full 3D simulation.

Here, σ_i, σ_j are 3-state variables defining the three different guest orientations and δ is a function which is -1 if $\sigma_i = \sigma_j$ and $+1$ otherwise. For the strain energy, we again define a radius, r_s, within which we attempt to maintain equal proportions of the different domains using

$$E_{\text{strain}} = K_s[(f_1 - \tfrac{1}{3})^2 + (f_2 - \tfrac{1}{3})^2 + (f_3 - \tfrac{1}{3})^2], \qquad (6)$$

where f_1, f_2, f_3 are the fractions of sites within a circle of radius r_s of a given site, which have the orientations 1, 2 or 3, respectively.

4.3. Simulation results for didecylbenzene/urea

Simulation was carried out for 200 MC cycles on a 2D hexagonal lattice consisting of 128×128 lattice sites. The temperature used in the simulation was given by $kT = 1.0$ and a suitable value of the strain constant K_s was found by trial and error to be 150. As for the CSZ example, the radius r_s was taken as $3\times$ the nearest-neighbour intermolecular distance. [Note that the constant K_s cannot be simply related to that used for the CSZ example because of the rather different form of (6) compared with (4).] A small representative portion of the resulting distribution is shown in Fig. 8(*d*). The different coloured circles (white, grey and black) each represents a

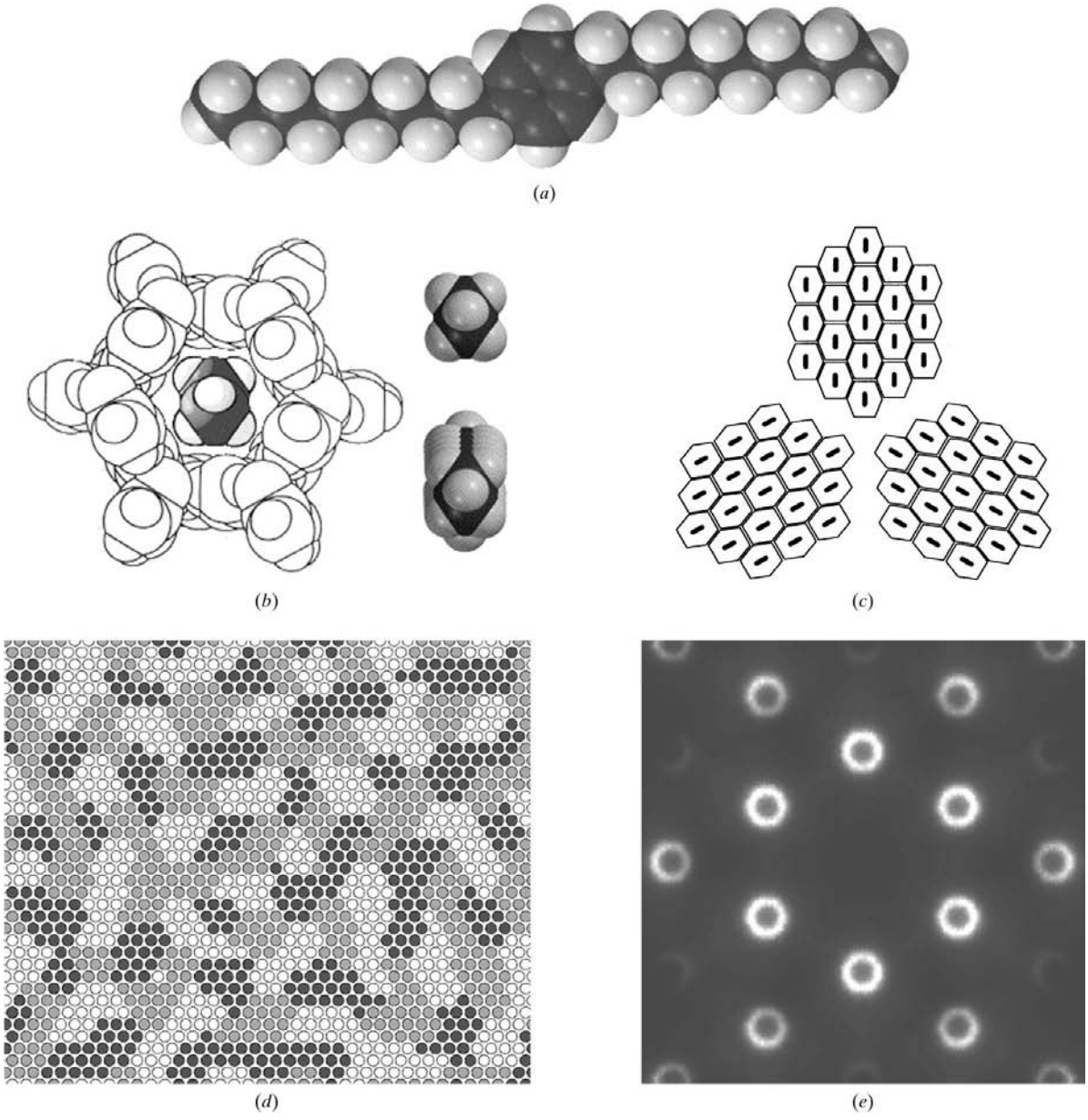

Figure 8
(*a*) Space-filling model of *p*-didecylbenzene molecule. (*b*) Urea channel containing the 'footprint' of an *n*-alkane molecule, together with a comparison of the 'footprints' of *n*-alkane and the didecylbenzene molecule. (*c*) Schematic view of three different orientations of the distorted (exaggerated) urea network when containing the didecylbenzene molecules. (*d*) Portion of distribution of three 'footprint' orientations resulting from MC simulation. The three shades of grey represent the three orientations shown in (*c*). (*e*) Diffraction pattern calculated from distribution shown in (*d*).

didecylbenzene molecule in one of the three orientations displayed in Fig. 8(*c*). Fig. 8(*e*) shows a diffraction pattern calculated from the distribution. To make this calculation, a simplified representation of the molecular scattering factor was used, which consisted of two pseudo-atoms forming a dumbbell shape similar to that used in Welberry & Mayo (1996). A more realistic molecular scattering factor would result in different relative intensities of the diffuse rings seen in the pattern, but would not affect the overall form of the pattern.

5. Diffuse 'hole' in 1,3-dibromo-2,5-diethyl-4,6-dimethylbenzene

5.1. Background

In the pure molecular crystal compound 1,3-dibromo-2,5-diethyl-4,6-dimethylbenzene, $C_{12}H_{16}Br_2$ (BEMB2), each molecular site may contain the molecule in one of two different orientations. The average structure as revealed by conventional Bragg reflection analysis is $P2_1/c$ with the 1,3- and 4,6-substituent sites containing 50% bromo- and 50% methyl-. The average molecular site is centrosymmetric so that the packing of molecular shapes shown schematically in Fig. 9(*a*) satisfies both the 2_1-screw axes and the *c*-glide planes. In the real crystal, where each site must be occupied by one or other of the two possible molecular orientations, either the 2_1-screw axis or the *c*-glide plane may be satisfied on a local scale but not both. Fig. 9(*b*) shows the arrangement where the 2_1-screw axis is satisfied, while for Fig. 9(*c*) it is the *c*-glide plane.

On a local level, intermolecular interactions are strongly influenced by the molecular dipoles that the molecules possess. In Fig. 9(*b*), these dipole moments are all approximately aligned with each other, giving an unfavourably high contribution to the interaction energy. In Fig. 9(*c*), the dipoles in the centre of the cell are approximately aligned antiparallel to those at the corners of the cell, giving a much more stable configuration. Locally, therefore, it appears that the molecules would prefer to form the structure (Fig. 9*c*) where the *c*-glide symmetry prevails.

Wilson (1988, 1990), following the pioneering work of Kitaigorodsky (1973), showed, however, that molecular shapes are more easily able to pack to form a stable crystal structure using screw axes rather than glide planes. This is borne out by the relative frequency with which the space groups $P2_1$ and Pc (the two subgroups of $P2_1/c$) occur, Pc being one of the space groups that occur very rarely in nature. From a crystal packing point of view, therefore, it is clear that for BEMB2 to pack in the *c*-glide conformation an energy penalty would result relative to the preferred (lowest-energy) $P2_1$ structure shown in Fig. 9(*b*).

The situation is thus entirely analogous to that in the two previous examples. At short distances, near-neighbour interactions are trying to make one kind of packing, but at slightly longer distances the strain energy builds up sufficiently that this arrangement is no longer viable and the structure cannot propagate further.

5.2. Monte Carlo simulation

To demonstrate the effect for BEMB2, we construct a simple 2D model corresponding to the *a*-axis projection of the structure. Each molecule in this basal plane is surrounded by eight neighbours involving three symmetry-unrelated vectors. In order to produce the preferred short-range-ordered structure, we assume that the local interaction energy is of the form

$$E_{\rm local} = \sum_{\rm neighbours} K_i \sigma_0 \sigma_i, \tag{7}$$

where σ_0, σ_i are $(-1, +1)$ binary random variables representing the orientation of the molecule on a given site 0 and its neighbour i, respectively. The three independent values of K_i, corresponding to the three symmetry-unrelated vectors shown in Fig. 9(*a*), were chosen by trial and error so that the diffraction pattern calculated from the model gave a qualitatively good agreement with the broad features of the observed diffuse scattering shown in Fig. 1(*d*).

In order to apply a strain term, we again use a circular region, radius r_s, around a given molecular site. In this case, we define the fractions of sites within this circle that are in orientation 1, f_1 is the fraction for sites on sublattice 1 (the corners of the unit cell) and f_2 is the fraction for sites on sublattice 2 (the centres of the unit cell). Then the form of the strain term, which attempts to keep the fraction of sites that are in orientation 1 equal on the two sublattices, that was used was

$$E_{\rm strain} = K_s (f_1 - f_2)^2. \tag{8}$$

In this case, it was necessary for the radius, r_s, to be much greater than for the previous two examples because the 'diffuse hole' in Fig. 1(*d*) is much smaller than the diffuse rings in Figs. 1(*b*) and 1(*c*). Initially, a radius of 15× the nearest-neighbour intermolecular distance was used. However, it was found that this not only gave a diffuse 'hole' as in the observed pattern but also a quite distinct ring of stronger scattering like a miniature version of the rings in Figs. 7(*e*) and 8(*e*). In order to overcome this, the form of (8) was changed to include a gradually graded strain by having similar terms that operated over circles of different radii.

$$E_{\rm strain} = K_{s1}(f_{11} - f_{12})^2 + K_{s2}(f_{21} - f_{22})^2 + K_{s3}(f_{31} - f_{32})^2. \tag{9}$$

The constants K_{s1}, K_{s2}, K_{s3} operated over circles of radius 10×, 12.5× and 15× the nearest-neighbour intermolecular distance and had the values 50, 100 and 200, respectively.

5.3. Simulation results for BEMB2

MC simulation was carried out on a 2D primitive square lattice of 512 × 512 sites. The sites of this primitive lattice were then mapped onto the body-centred crystal lattice so that a cell edge of the primitive lattice corresponded to the nearest-neighbour intermolecular distance in the crystal lattice. 100 cycles of iteration were performed during which fixed values of the strain constants K_{s1}, K_{s2}, K_{s3} were used but the short-range-order constants of K_i were adjusted using a feedback

mechanism in order to achieve predetermined values for near-neighbour short-range-order parameters (correlation coefficients). These values, which gave good qualitative agreement with the observed pattern, were chosen to be:

$C_1 = -0.4$ between molecules at the corners and centres of the unit cell. The negative value indicates a strong tendency for the *c*-glide local configuration.

$C_2 = +0.4$ between molecules separated by a whole *c* cell repeat. The positive correlation indicates a tendency for neighbouring cells in this direction to be the same. This results in the diffuse scattering being concentrated in bands normal to $[10\bar{1}]^*$.

$C_3 = 0.0$ between molecules separated by a whole *b* cell repeat. Although having a zero value, this represents a quite

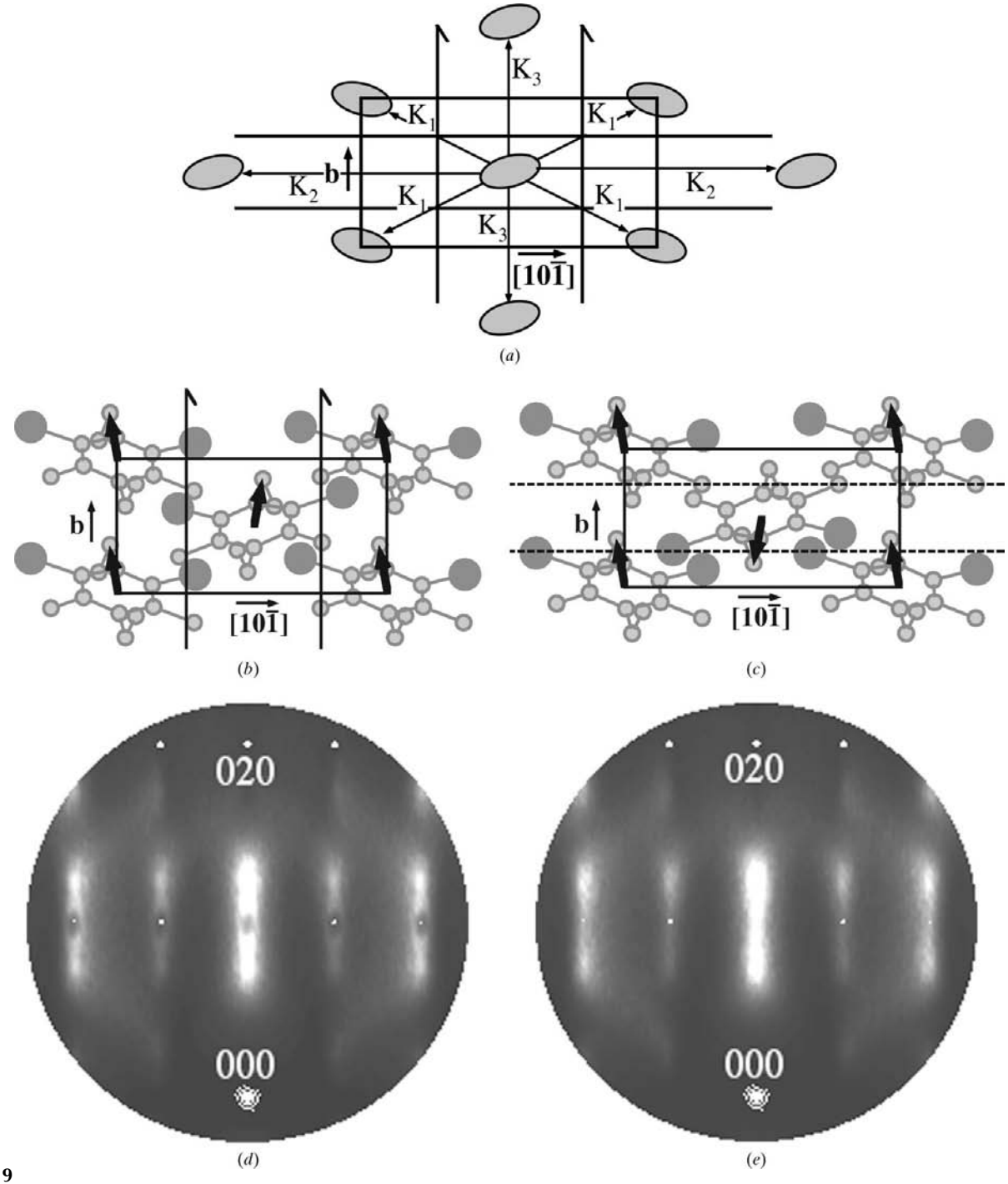

Figure 9
(*a*) Schematic drawing of the molecular packing of centrosymmetric molecules corresponding to the average structure of BEMB2. (*b*) Local packing of BEMB2 molecules satisfying the 2_1-screw axis. (*c*) Local packing of BEMB2 molecules satisfying the *c*-glide plane. (*d*) Diffraction pattern calculated from the MC simulation which included strain. (*e*) Diffraction pattern calculated from the MC simulation without strain. In (*b*) and (*c*), the small dark arrows indicate the direction of the molecular dipoles.

strong restraint to the nearest-neighbour C_1 correlation propagating along **b**. The zero value gives the strong diffuse band near the centre of the pattern the elongated rather flat-topped appearance.

The final diffraction pattern calculated from the model including both SRO and strain is shown in Fig. 9(*d*). Note that the diffuse 'hole' appears around all Bragg positions including the systematically absent (010). Fig. 9(*e*) shows the corresponding pattern for the model without the strain term.

6. Conclusions

We have shown in this paper that a feature that has been observed in the diffuse scattering patterns of a wide variety of different materials – a diffuse 'ring' or 'doughnut'-shaped region of scattering – can be understood in terms of a simple model that has been borrowed from the field of sol–gel science. In this it is supposed that there is a balance between the local attractive forces that are trying to make a particular structure and a rather longer range repulsive force. In the present context, we believe this latter force has its origin in the strain that builds as the preferred local structure tries to fit into the average crystal lattice. We have described here simple MC models in which this principle has been demonstrated for three examples: cubic stabilized zirconia, the didecylbenzene/urea inclusion compound and the pure molecular compound 1,3-dibromo-2,5-diethyl-4,6-dimethylbenzene (BEMB2). A similar feature is also observed in the aluminosilicate ceramic mullite. Although we are confident that this feature in mullite has similar origins to those of the other examples described, no attempt has been made to model it at this stage as this system shows additional incommensurate diffraction effects not easily described by the kind of simple model presented here.

The result of the present work is particularly important in the context of the stabilized zirconia problem. The realisation that the very complex structural problem can be explained by such a simple physical idea should enable further progress to be made in understanding the properties of a wide range of these materials. A description in terms of the cation ordering is, from a chemical point of view, a much more natural approach than that used in previous studies where the oxygen vacancies were given prominence. To incorporate the anions into the derived cation, distributions should be quite feasible using simple bond-valence criteria, so that a much more complete model should now be accessible. Further work on this system is in progress.

It is important to point out that the potentials used in the present work are simple approximations invented for the sole purpose of demonstrating the effect of current interest and they should not be taken out of context. For example, we are not suggesting that the pyrochlore lattice energy is only dependent on the cation clusters shown in Fig. 5(*d*). The potential involving these clusters merely provided a simple means of generating a pyrochlore lattice using only near-neighbour interactions. Similarly, the device we used in all three examples, of applying a strain energy *via* a constraint of a particular lattice average over a circular domain, was adopted for simplicity and convenience only. A more rigorous treatment would clearly need to involve proper interatomic interactions between all atoms over a large distance range [*e.g.* equation (2)], and would necessarily be more computer intensive for real systems than currently feasible.

References

Allpress, J. G. & Rossell, H. J. (1975). *J. Solid State Chem.* **15**, 68–78.
Butler, B. D. & Hanley, H. J. M. (1999). *J. Sol–Gel Sci. Technol.* **15**, 161–166.
Butler, B. D. & Welberry, T. R. (1992). *J. Appl. Cryst.* **25**, 391–399.
Butler, B. D. & Welberry, T. R. (1994). *J. Appl. Cryst.* **27**, 742–754.
Cahn, J. W. (1967). *Trans. Metallurg. Soc. Am.* **242**, 168–180.
Kitaigorodsky, A. I. (1973). *Molecular Crystals and Molecules.* New York: Academic Press.
Mayo, S. C., Welberry, T. R., Bown, M. & Tarr, A. (1998). *J. Solid State Chem.* **141**, 437–451.
Morinaga, M., Cohen, J. B. & Faber, J. (1980). *Acta Cryst.* A**36**, 520–530.
Neder, R. B., Frey, F. & Schultz, H. (1990). *Acta Cryst.* A**46**, 799–809.
Rossell, H. J. & Scott, H. G. (1977). *J. Phys. (Paris) Colloq.* C7, no 12, **38**, 28–31.
Suzuki, S., Tanaka, M. & Ishigame, M. (1985). *Jpn. J. Appl. Phys.* **24**, 401–410.
Welberry, T. R., Butler, B. D., Thompson, J. G. & Withers, R. L. (1993). *J. Solid State Chem.* **106**, 461–475.
Welberry, T. R. & Mayo, S. C. (1996). *J. Appl. Cryst.* **29**, 353–364.
Welberry, T. R. & Siripitayananon, J. (1987). *Acta Cryst.* B**43**, 97–106.
Welberry, T. R. & Withers, R. L. (1990). *Phys. Chem. Miner.* **17**, 117–124.
Welberry, T. R., Withers, R. L. & Mayo, S. C. (1995). *J. Solid State Chem.* **115**, 43–54.
Wilson, A. J. C. (1988). *Acta Cryst.* A**44**, 715–724.
Wilson, A. J. C. (1990). *Acta Cryst.* A**46**, 742–754.